

The Principles of STEM Imaging

Peter D. Nellist

2.1 Introduction

The purpose of this chapter is to review the principles underlying imaging in the scanning transmission electron microscope (STEM). Consideration of interference between parts of the convergent illuminating beam will be used to provide a common framework which allows contrast in various modes to be considered, and serves to allow the resolution limits of imaging to be determined. Several of the other chapters in this volume deal with specific imaging modes, so we do not seek to provide a detailed analysis of all those modes here, rather we will point out how these imaging modes may be considered in similar ways.

Figure 2–1 shows a schematic of the STEM optical configuration. A series of lenses focuses a beam to form a small spot, or probe, incident upon a thin, electron-transparent sample. Except for the final focusing lens, which is referred to as the objective, the other pre-sample lenses are referred to as condenser lenses. The aim of the lens system is to provide enough demagnification of the finite-sized electron source in order to form an atomic-scale probe at the sample. The objective lens provides the final, and largest, demagnification step. It is the aberrations of this lens that dominate the optical system. An objective aperture is used to restrict its numerical aperture to a size where the aberrations do not lead to significant blurring of the probe. The requirement of an objective aperture has two important consequences: (i) it imposes a diffraction limit to the smallest probe diameter that may be formed and (ii) electrons that do not pass through the aperture are lost, and therefore the aperture restricts the amount of beam current available.

Scan coils are arranged to scan the probe over the sample in a raster, and a variety of scattered signals can be detected and plotted as a function of probe position to form a magnified image. There is a wide range of possible signals available in the STEM, but the commonly collected ones are the following

- (i) Transmitted electrons that leave the sample at relatively low angles with respect to the optic axis (smaller than the incident beam convergence angle). This mode is referred to as bright field (BF).

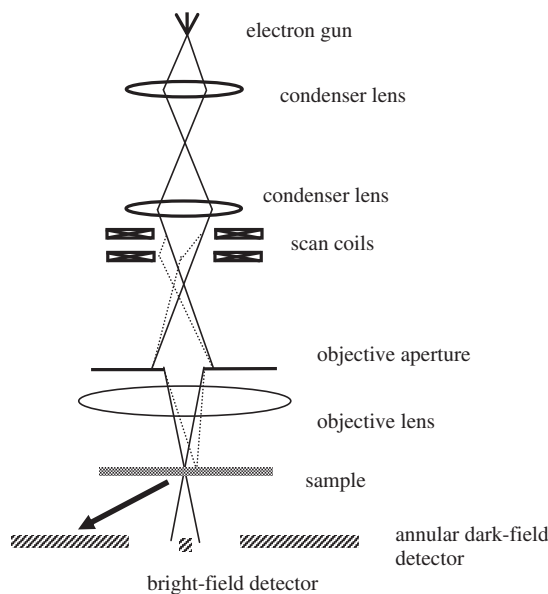


Figure 2–1. A schematic diagram of a STEM instrument showing the elements discussed in this chapter.

- (ii) Transmitted electrons that leave the sample at relatively high angles with respect to the optic axis (usually at an angle several times the incident beam convergence angle). This mode is referred to as annular dark field (ADF).
- (iii) Transmitted electrons that have lost a measurable amount of energy as they pass through the sample. Forming a spectrum of these electrons as a function of the energy lost leads to electron energy loss spectroscopy (EELS).
- (iv) X-rays generated from electron excitations in the sample (EDX).

Post-specimen optics may also be present to control the angles subtended by some of these detectors, but such optics play no part in the image formation process and will not be considered here.

In this chapter we will mainly consider the first two detection modes on the above list. Chapter 6 deals more extensively with quantitative ADF imaging calculations and imaging using inelastically scattered electrons and Chapter 7 deals with EDX mapping.

2.2 The Principle of Reciprocity

Before embarking on a discussion of the origins of contrast and resolution limits in STEM imaging, it is first important to consider the implications of the *principle of reciprocity*. Consider elastic scattering so that all the electron waves in the microscope have the same energy. Under these conditions, the propagation of the electrons is time reversible. Points in the original detector plane could be replaced with electron sources, and the original source replaced with a detector, and a similar

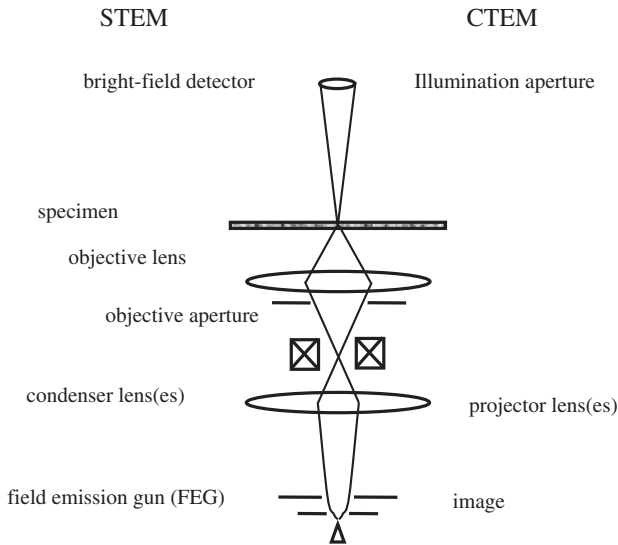


Figure 2–2. A schematic diagram showing the equivalence between bright-field STEM and HRTEM imaging making use of the principle of reciprocity.

intensity would be seen. Applying this concept to STEM (Cowley 1969, Zeitler and Thomson 1970), it becomes clear that the STEM imaging optics (before the sample) are equivalent to the imaging optics (after the sample) in the conventional TEM (CTEM). Similarly, the detector plane in STEM plays a similar role to the illumination configuration in CTEM.

We will see later that many of the concepts relating to coherence derived for CTEM can be transferred to STEM making use of the principle of reciprocity. As an immediate illustration of reciprocity, consider simple bright-field (BF) imaging. In the CTEM the ideal situation is that the sample is illuminated by perfectly coherent plane-wave illumination, and post-specimen optics form a highly magnified image of the wave that is transmitted by the sample. Now reverse this process to reveal the BF configuration for STEM (Figure 2–2). The electron source in the STEM plays an equivalent role to an image pixel in CTEM. The STEM imaging optics form a highly demagnified image of the source at the sample, and that can be scanned over the sample. Plane-wave transmission is then detected, usually with a small detector placed on the optic axis in the far field, and plotted as a function of probe position. The principle of reciprocity suggests that the image contrast will have the same form in both the CTEM and STEM cases, and this is observed experimentally (Crewe and Wall 1970) (see Figure 1–5). In the rest of this chapter, we will derive the imaging attributes from the STEM point of view but make the connection to CTEM where appropriate.

2.3 Interference Between Overlapping Discs

The origins of contrast in STEM arise from the interference between partial plane waves in the convergent beam that form the probe. Many

such beams can interfere as they are scattered into the final beam that propagates to the detector, leading to a change in the intensity of this final beam as the probe is moved and hence image contrast (Spence and Cowley 1978). To understand this process, it is instructive to first consider lattice imaging of a simple sample that only scatters to reciprocal lattice vectors \mathbf{g} and $-\mathbf{g}$ in addition to transmitting an unscattered beam. Plane-wave illumination of such a sample would lead to three spots: the direct beam and the two scattered beams. In STEM we have a coherent convergent beam illuminating the sample, and so the diffracted beams broaden to form discs. Where these diffracted discs overlap, interference features will be seen, and it is these interference features that lead to image contrast in STEM (Figure 2–3). To explain the form of these interference features, we need to follow the wavefunction through the microscope.

We start by assuming that the front focal plane of the objective lens is coherently illuminated. We assume that the effects of aberrations can be treated as a phase shift χ that has the form

$$\chi(\mathbf{K}) = \left(\pi C_{1,0} \lambda |\mathbf{K}|^2 + \frac{1}{2} \pi C_{3,0} \lambda^3 |\mathbf{K}|^4 \right), \quad (1)$$

where we have considered only defocus $C_{1,0}$ and spherical aberration $C_{3,0}$ as being present, and \mathbf{K} is the transverse component of the wavevector at that position in the front focal plane. In an aberration-corrected microscope, the instrument will not be limited by $C_{3,0}$, and the general aberration phase surface is given in Chapters 3 and 7. To limit the influence of aberrations, an aperture is used, allowing beams to contribute up to a maximum transverse wavevector $K_{\max} = \lambda/\alpha$; thus the

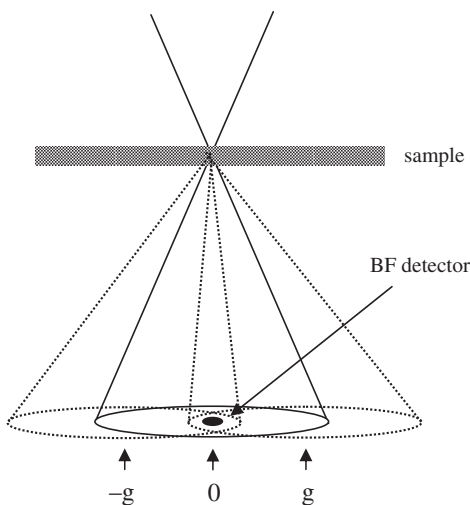


Figure 2–3. Diffraction of the coherent convergent beam by a specimen leads to diffracted discs. Where these discs overlap, interference will be seen. The bright-field detector is sensitive to interference between the direct beam and the two opposite diffracted beams.

overall wave at the front focal plane is given by the lens transmission function

$$T(\mathbf{K}) = A(\mathbf{K}) \exp[-i\chi(\mathbf{K})], \quad (2)$$

where A is a function that describes the size of the objective aperture, having a value of 1 for $|\mathbf{K}| \leq K_{\max}$ and 0 elsewhere.

The electron probe can now be calculated by simply taking the inverse Fourier transform of the wave at the front focal plane, thus

$$P(\mathbf{R}) = \int T(\mathbf{K}) \exp(i2\pi \mathbf{K} \cdot \mathbf{R}) d\mathbf{K}. \quad (3)$$

To express the ability of the STEM to move the probe over the sample, we can include a shift term in Eq. (3) to give

$$P(\mathbf{R} - \mathbf{R}_0) = \int T(\mathbf{K}) \exp(i2\pi \mathbf{K} \cdot \mathbf{R}) \exp(-i2\pi \mathbf{K} \cdot \mathbf{R}_0) d\mathbf{K}, \quad (4)$$

where \mathbf{R}_0 is the probe position. Moving the probe is therefore equivalent to adding a linear ramp to the phase variation across the front focal plane, which is exactly what the scan coils do.

Now consider diffraction by a sample. If we assume a thin sample that can be treated as being a thin, multiplicative transmission function, ϕ , then the wave exiting the sample can be written as

$$\psi(\mathbf{R}, \mathbf{R}_0) = P(\mathbf{R} - \mathbf{R}_0)\phi(\mathbf{R}). \quad (5)$$

To calculate the wave at the detector plane, we take the Fourier transform of Eq. (5). Because Eq. (5) is a product, its Fourier transform becomes a convolution and can be written as

$$\psi(\mathbf{K}_f, \mathbf{R}_0) = \int \phi(\mathbf{K}_f - \mathbf{K}) T(\mathbf{K}) \exp(-i2\pi \mathbf{K} \cdot \mathbf{R}_0) d\mathbf{K}, \quad (6)$$

where changes in the argument of a function to reciprocal space vectors indicate that the Fourier transform has been taken. This equation has a relatively simple interpretation. The detector is in diffraction space, and the wave incident upon the detector at a position corresponding to a transverse wavevector \mathbf{K}_f , is the sum of all waves incident upon the sample, with transverse wavevectors \mathbf{K} , that are scattered by the object to \mathbf{K}_f . Now consider a sample that transmits a direct beam and scatters into $+\mathbf{g}$ and $-\mathbf{g}$ beams, i.e. it contains only a simple sinusoidal variation, either in amplitude or phase. The Fourier transform of the sample transmission function will contain Dirac delta functions at $\mathbf{0}$, $-\mathbf{g}$ and $+\mathbf{g}$. Substituting this form into Eq. (6) gives

$$\begin{aligned} \psi(\mathbf{K}_f, \mathbf{R}_0) = & T(\mathbf{K}) \exp[-i2\pi \mathbf{K} \cdot \mathbf{R}_0] + \phi_{\mathbf{g}} T(\mathbf{K} - \mathbf{g}) \exp[-i2\pi (\mathbf{K} - \mathbf{g}) \cdot \mathbf{R}_0] \\ & + \phi_{-\mathbf{g}} T(\mathbf{K} + \mathbf{g}) \exp[-i2\pi (\mathbf{K} + \mathbf{g}) \cdot \mathbf{R}_0], \end{aligned} \quad (7)$$

where $\phi_{\mathbf{g}}$ represent the complex amplitude (amplitude and phase) of the beam scattered to $+\mathbf{g}$. Because T has an amplitude that is disc shaped

(being controlled by the shape and size of the objective aperture), the form of the diffraction pattern will be three discs. If the objective aperture is large enough, the discs will overlap, as shown for example in Figure 2-3. Where the discs overlap, coherent interference can occur (Cowley 1979 1981, Spence 1992). To examine the form of the interference in the region where only the $\mathbf{0}$ and $+\mathbf{g}$ discs overlap, we need to calculate the intensity in this region. Taking the modulus squared of Eq. (7) and only considering the $\mathbf{0}$ and $+\mathbf{g}$ terms, which are the only ones contributing in this region, gives

$$I(\mathbf{K}_f, \mathbf{R}_0) = 1 + |\phi_g|^2 + 2|\phi_g|\cos[-\chi(\mathbf{K}_f) + \chi(\mathbf{K}_f - \mathbf{g}) + 2\pi\mathbf{g} \cdot \mathbf{R}_0 + \angle\phi_g], \quad (8)$$

where $\angle\phi_g$ is the phase of the beam diffracted to $+\mathbf{g}$.

Equation (8) reveals features of the interference that are important for understanding STEM imaging:

- (i) The intensity in the overlap region varies sinusoidally as the probe is scanned. If a point detector was placed in this region and used to form a STEM image, fringes would be seen in the image corresponding to the spacing of the sample, and their geometric position is controlled by the phase relationship of the interfering beams.
- (ii) Lens aberration can also affect the form in this overlap region. Consider just defocus (i.e. ignoring all other aberrations). Using Eq. (2) it is possible to evaluate the quantity

$$-\chi(\mathbf{K}_f) + \chi(\mathbf{K}_f - \mathbf{g}) = \pi z \lambda \left[-\mathbf{K}_f^2 + (\mathbf{K}_f - \mathbf{g})^2 \right] = \pi z \lambda \left[-2\mathbf{K}_f \cdot \mathbf{g} + |\mathbf{g}|^2 \right]. \quad (9)$$

This quantity is linear in \mathbf{K}_f , and so substituting it into Eq. (8) reveals that a uniform set of fringes will be seen running perpendicular to the \mathbf{g} vector. Such a set of interference fringes are seen in Figure 2-4. Although these fringes exist in diffraction space, their spacing, as specified in diffraction angle, corresponds to the spacing in the sample divided by the value of the defocus. Thus they can be thought of as a shadow image of the lattice in the sample. This illustrates how the detector plane in STEM, albeit nominally in diffraction space, can show real-space information. Removing the aperture completely gives an electron Ronchigram (see Chapter 3). As the defocus is reduced to zero, the apparent magnification of the shadow increases until at zero defocus the shadow has infinite magnification, and the disc overlap region contains a uniform intensity.

If we now include higher order aberrations rather than just defocus, such as spherical aberration, the form of the interference features will become more complicated. The fringes will distort, and it will not be possible to fill the overlap region with a uniform intensity.

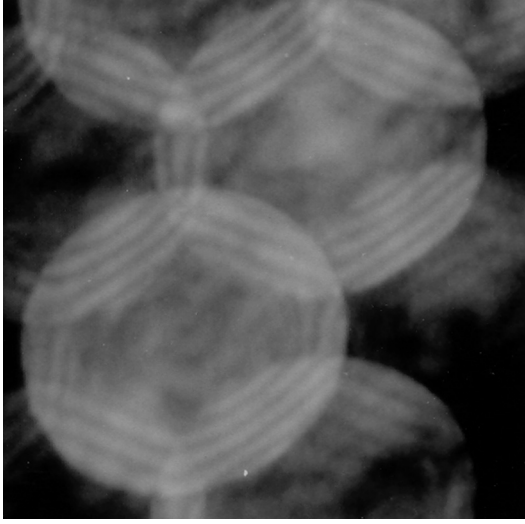


Figure 2-4. Overlapping diffracted discs in a coherent convergent-beam electron diffraction pattern. The probe has been defocused leading to relatively fine interference features in the disc overlap regions.

2.4 Bright-Field Imaging

As mentioned previously, reciprocity shows that the STEM equivalent of CTEM imaging is to use a small detector on the optic axis. From Figure 2-3 it can be seen that such a detector makes use of the intensity in a triple overlap region where the direct $\mathbf{0}$ beam and the $+\mathbf{g}$ and $-\mathbf{g}$ beams overlap. The wavefunction at this point is given by

$$\begin{aligned} \Psi(\mathbf{K}_f = \mathbf{0}, \mathbf{R}_0) = & 1 + \phi_{\mathbf{g}} \exp[-i\chi(-\mathbf{g}) - i2\pi\mathbf{g} \cdot \mathbf{R}_0] \\ & + \phi_{-\mathbf{g}} \exp[-i\chi(\mathbf{g}) + i2\pi\mathbf{g} \cdot \mathbf{R}_0]. \end{aligned} \quad (10)$$

Taking the modulus squared of Eq. (10) and neglecting terms of higher order than linear gives

$$\begin{aligned} I(\mathbf{K}_f = \mathbf{0}, \mathbf{R}_0) = & 1 + \phi_{\mathbf{g}} \exp[-i\chi(-\mathbf{g}) - i2\pi\mathbf{g} \cdot \mathbf{R}_0] \\ & + \phi_{-\mathbf{g}} \exp[-i\chi(\mathbf{g}) + i2\pi\mathbf{g} \cdot \mathbf{R}_0] \\ & + \phi_{\mathbf{g}}^* \exp[i\chi(-\mathbf{g}) + i2\pi\mathbf{g} \cdot \mathbf{R}_0] \\ & + \phi_{-\mathbf{g}}^* \exp[i\chi(\mathbf{g}) - i2\pi\mathbf{g} \cdot \mathbf{R}_0]. \end{aligned} \quad (11)$$

Now consider a weak-phase object where we can write

$$\phi_{\mathbf{g}} = i\sigma V_{\mathbf{g}} \quad (12)$$

where $V_{\mathbf{g}}$ is the \mathbf{g} th Fourier component of the specimen potential. Because the potential is real,

$$V_{\mathbf{g}}^* = V_{-\mathbf{g}}, \quad (13)$$

and therefore

$$\begin{aligned}
 I(\mathbf{K}_f = 0, \mathbf{R}_p) = & 1 + i\sigma V_g \exp i[-\chi(-\mathbf{g}) - 2\pi \mathbf{g} \cdot \mathbf{R}_0] \\
 & + i\sigma V_g^* \exp i[-\chi(\mathbf{g}) + 2\pi \mathbf{g} \cdot \mathbf{R}_0] \\
 & - i\sigma V_g^* \exp i[\chi(-\mathbf{g}) + 2\pi \mathbf{g} \cdot \mathbf{R}_0] \\
 & - i\sigma V_g \exp i[\chi(\mathbf{g}) - 2\pi \mathbf{g} \cdot \mathbf{R}_0].
 \end{aligned} \tag{14}$$

Collecting terms and assuming that χ is a symmetric function,

$$\begin{aligned}
 I_{\text{BF}}(\mathbf{R}_p) = & 1 + i(\exp[-i\chi(\mathbf{g})] - \exp[i\chi(\mathbf{g})]) \\
 & \times (\sigma V_g \exp[-i2\pi \mathbf{g} \cdot \mathbf{R}_0] + \sigma V_g^* \exp[i2\pi \mathbf{g} \cdot \mathbf{R}_0]) \\
 = & 1 + 2\sigma \sin(\chi(\mathbf{g})) [|V_g| \exp(-i2\pi \mathbf{g} \cdot \mathbf{R}_0 + \angle V_g) \\
 & + |V_g| \exp[i2\pi \mathbf{g} \cdot \mathbf{R}_0 - \angle V_g]],
 \end{aligned} \tag{15}$$

which simplifies to give

$$I_{\text{BF}}(\mathbf{R}_0) = 1 + 4|\sigma V_g| \cos(2\pi \mathbf{g} \cdot \mathbf{R}_0 - \angle V_g) \sin \chi(\mathbf{g}), \tag{16}$$

which is the standard form of phase contrast imaging in the electron microscope (Spence 1988), with the phase contrast transfer function being given by $\sin(\chi)$.

Thus BF imaging in STEM shows the usual phase contrast imaging, with a phase contrast transfer function that is controlled by the lens aberrations, in a similar way to phase contrast imaging in CTEM. The principle of reciprocity is thereby confirmed. It should be pointed out, however, that BF imaging in STEM is much less efficient of electrons than that in CTEM because the small detector does not collect the majority of the electrons in the detector plane.

2.5 Resolution Limits

Figure 2–3 shows that triple overlap conditions can occur only if the magnitude of \mathbf{g} is less than the radius of the aperture. The aperture itself is used to prevent highly aberrated rays contributing to the image (which in the bright-field model would correspond to the oscillatory region of the phase contrast transfer function). If the magnitude of \mathbf{g} has a value lying between the aperture radius and the aperture diameter, there will still be interference in the single overlap regions (see Figure 2–5). Thus information at this resolution can be recorded in a STEM, but not using an axial detector. An off-axis detector needs to be used to record this so-called single sideband interference. By reciprocity, the equivalent approach in HRTEM is to use tilted illumination, which has been shown to improve image resolution (Haigh et al. 2009).

Ideas for making use of this single sideband interference include differential phase contrast detectors (Dekkers and de Lang 1974) and annular bright-field detectors (Rose 1974). It can also be seen that an

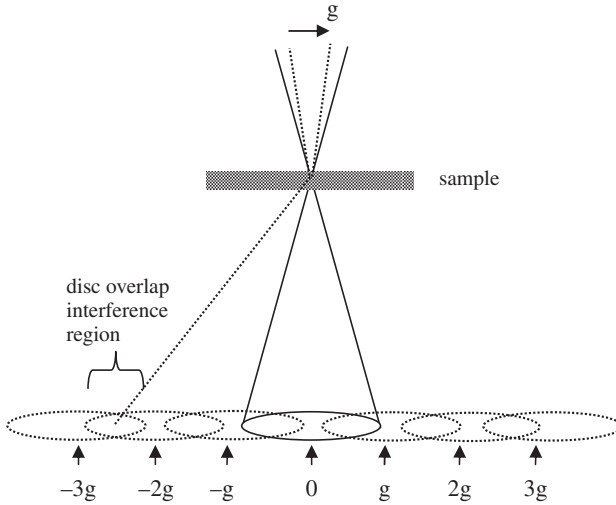


Figure 2-5. For smaller lattice spacings, the triple overlap regions necessary for bright-field STEM may not exist and no contrast will be seen. Such spacings can be resolved, however, using non-axial detector geometries including annular dark field.

annular dark-field detector would also detect single overlap interference, though at the angles usually detected, discrete discs are no longer observable because of the effects of thermal diffuse scattering.

A broad statement for STEM resolution is that for a spatial frequency Q to show up in the image, two beams incident on the sample separated by Q must be scattered by the sample so that they end up in the same final wavevector K_f where they can interfere. This model of STEM imaging is applicable to any imaging mode, even when TDS or inelastic scattering is included. We can immediately conclude that STEM is unable to resolve any spacing smaller than that allowed by the diameter of the objective aperture, no matter which imaging mode is used.

2.6 Partial Coherence in STEM Imaging and the Need for Brightness

The models so far presented have assumed that the illuminating electron beam emanates from a point source (has perfect spatial coherence), is perfectly monochromatic (has perfect temporal coherence) and that the BF detector is infinitesimal. Coherence is used to model the degree to which different beams can interfere, therefore the effects of partial coherence can strongly influence the form of STEM images. Let us consider each in turn.

2.6.1 Source Spatial Coherence and Brightness

Any electron gun emits radiation from a finite-size source, which is regarded to be self-luminous. Radiation emitted from one point is

assumed to be unable to interfere with the radiation from any neighbouring point. To model this coherence, we can treat each point in the electron source as giving rise to its own illuminating probe at the sample. For each desired probe position, corresponding to a pixel in the image, the detected image intensity arises from a range of actual probe positions that are then added. This can be described by a convolution, and it can be written as

$$I_{\text{src}}(\mathbf{R}_0) = I(\mathbf{R}_0) \otimes S(\mathbf{R}_0), \quad (17)$$

where S is the source intensity distribution as measured at the sample plane, i.e. after taking source demagnification into account.

It is immaterial how the nominally coherent image $I(\mathbf{R}_0)$ is formed, the effects of partial source coherence can always be modelled as a simple convolution of the image with the effective source size. The purpose of condenser lenses is to demagnify the electron source as much as possible to reduce the deleterious effects of partial source coherence. The more the source is demagnified, the lower the current in the probe, as shown in Figure 2–6. The crucial quantity is brightness B , which is defined as the current per unit area per unit solid angle subtended by the beam. Brightness is conserved in an optical system, and so knowledge of the brightness of the electron source allows calculation of the current available in the STEM probe. Given that the solid angle subtended by the incident beam is controlled by the size of the objective aperture, it is possible to write the current available in the probe J in terms of the probe diameter d and the brightness B :

$$J = B\pi^2\alpha^2d^2/4. \quad (18)$$

Thus the smaller the STEM probe, the lower the current available and the higher the brightness needed to provide a reasonable current. It is for this reason that the development of the modern STEM required the development of a high-brightness gun (Crewe et al. 1968).

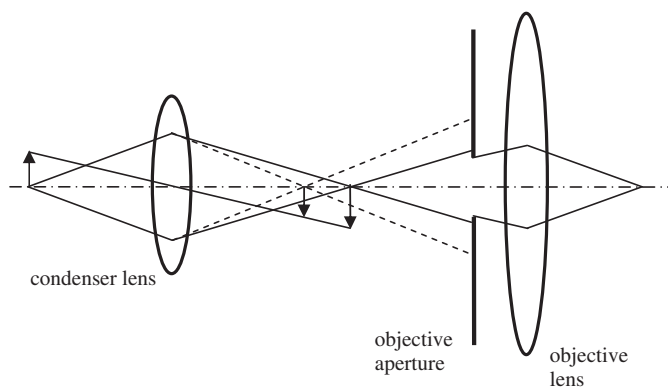


Figure 2–6. Increasing the strength of the condenser lens to provide greater source demagnification leads to greater loss of current at the objective aperture and less probe current.

2.6.2 Partial Detector Spatial Coherence

It might be considered strange to think of the effects of finite detector size as being regarded as a partial coherence. Clearly detectors do not affect the beam. However, a finite-sized detector might not detect very small interference features, and coherence refers to the ability to observe interference effects. Furthermore, by reciprocity a finite-sized detector in STEM is equivalent to a finite source in CTEM, and the latter would be conventionally regarded as a source of partial coherence.

The effects of partial detector coherence depend very much on the STEM imaging mode. For BF imaging, it leads to a coherence envelope similar to that seen for partial source coherence in CTEM (Nellist and Rodenburg 1994). It has a dependence on the slope of the aberration function χ and the reason for this becomes clear when one considers the interference in disc overlap regions. Aberrations will lead to smaller interference features in the overlap region and may therefore not be detected by a finite-sized detector.

It might be assumed that as the detector becomes larger, the effects of decreased coherence lead to weaker image contrast. Although it is indeed the case that the imaging process does become incoherent, the image contrast can be maintained, which brings us to the concept of incoherent imaging using an annular dark-field detector.

2.6.3 Partial Temporal Coherence

One of the important advantages of STEM is that all the imaging optics are placed before the sample, and optics after the sample do not influence the imaging process except for allowing the collection angles of detectors to be varied (essentially by changing the camera length of the post-specimen diffraction). The effects of temporal coherence arise from the finite energy spread of the beam, and the chromatic aberrations of the lenses. In CTEM, the energy spread can arise from inelastic scattering in the sample and can be broad. In STEM, partial temporal coherence can arise only because of the spread in energies of the illuminating beam, which is likely to be relatively low given that field emission sources are used.

Again, the exact effect of partial temporal coherence depends on the imaging mode being used. For BF imaging, the effect is similar to that for CTEM by reciprocity (Nellist and Rodenburg 1994), but for incoherent imaging modes, the effect of partial temporal coherence is not as severe (Nellist and Pennycook 1998).

2.7 Annular Dark-Field Imaging

The use of an annular dark-field (ADF) detector gave rise to one of the first detection modes used by Crewe and co-workers during the initial development of the modern STEM (Crewe 1980). The detector consists of an annular sensitive region that detects electrons scattered over an

angular range with an inner radius that may be a few tens of milliradians up to perhaps 100 mrad and an outer radius of several hundred milliradians. It has remained by far the most popular STEM imaging mode. It was later proposed that high scattering angles (~ 100 mrad) would enhance the compositional contrast (Treacy et al. 1978) and that the coherent effects of elastic scattering could be neglected because the scattering was almost entirely thermally diffuse (Howie 1979). This idea led to the use of the high-angle annular dark-field detector (HAADF). In this chapter, we will consider scattering over all angular ranges and will refer to the technique generally as ADF STEM.

It is indeed the case that for typical ADF detector angles, the scattering predominantly detected will be TDS. To understand the nature of incoherent imaging, and the resolution limits that apply, it is useful to first consider a lattice with no thermal vibrations so that the overlapping disc model used earlier applies. Figure 2-5 shows that an ADF detector will not only sum the intensity over entire disc overlap regions but also sum the intensity over many of such overlap regions. It might be expected that such an approach would generally wash out most of the available image contrast, but somewhat surprisingly this is not the case. The approach we take below follows very closely previous approaches (Jesson and Pennycook 1993, Loane et al. 1992, Nellist and Pennycook 1998).

Consider a sample that is continuous in Fourier space. An equivalent to Eq. (6) can be formed, the modulus squared taken to form an intensity, and that intensity then integrated over a detector function:

$$I_{\text{ADF}}(\mathbf{R}_0) = \int D_{\text{ADF}}(\mathbf{K}_f) \times \left| \int \phi(\mathbf{K}_f - \mathbf{K}) T(\mathbf{K}) \exp(-i2\pi \mathbf{K} \cdot \mathbf{R}_0) d\mathbf{K} \right|^2 d\mathbf{K}_f. \quad (19)$$

Taking the Fourier transform, after expanding the modulus squared, gives

$$I_{\text{ADF}}(\mathbf{Q}) = \int \exp(-i2\pi \mathbf{Q} \cdot \mathbf{R}_0) \int D_{\text{ADF}}(\mathbf{K}_f) \times \left\{ \int \phi(\mathbf{K}_f - \mathbf{K}) T(\mathbf{K}) \exp(-i2\pi \mathbf{K} \cdot \mathbf{R}_0) d\mathbf{K} \right\} \times \left\{ \int \phi^*(\mathbf{K}_f - \mathbf{K}') T^*(\mathbf{K}') \exp(i2\pi \mathbf{K}' \cdot \mathbf{R}_0) d\mathbf{K}' \right\} d\mathbf{K}_f d\mathbf{R}_0. \quad (20)$$

Performing the \mathbf{R}_0 integral first results in a Dirac δ function:

$$I_{\text{ADF}}(\mathbf{Q}) = \iiint D_{\text{ADF}}(\mathbf{K}_f) \phi(\mathbf{K}_f - \mathbf{K}) T(\mathbf{K}) \phi^*(\mathbf{K}_f - \mathbf{K}') \times T^*(\mathbf{K}') \delta(\mathbf{Q} + \mathbf{K} - \mathbf{K}') d\mathbf{K}_f d\mathbf{K} d\mathbf{K}', \quad (21)$$

which allows simplification by performing the \mathbf{K}' integral:

$$I_{\text{ADF}}(\mathbf{Q}) = \iint D_{\text{ADF}}(\mathbf{K}_f) T(\mathbf{K}) T^*(\mathbf{K} + \mathbf{Q}) \times \phi(\mathbf{K}_f - \mathbf{K}) \phi^*(\mathbf{K}_f - \mathbf{K} - \mathbf{Q}) d\mathbf{K}_f d\mathbf{K}. \quad (22)$$

Equation (22) is straightforward to interpret in terms of interference between diffracted discs (Figure 2-5). The integral over \mathbf{K} is a convolution so that Eq. (22) could be written as

$$I_{\text{ADF}}(\mathbf{Q}) = \int D_{\text{ADF}}(\mathbf{K}) \{ [T(\mathbf{K})T^*(\mathbf{K} + \mathbf{Q})] \otimes_{\mathbf{K}} [\phi(\mathbf{K})\phi^*(\mathbf{K} - \mathbf{Q})] \} d\mathbf{K}. \quad (23)$$

The first bracket of the convolution is the overlap product of two apertures, and this is then convolved with a term that encodes the interference between scattered waves separated by the image spatial frequency \mathbf{Q} . For a crystalline sample, $\phi(\mathbf{K})$ will only have values for discrete \mathbf{K} values corresponding to the diffracted spots. In this case Eq. (23) is easily interpretable as the sum over many different disc overlap features that are within the detector function.

We can expect that the aperture overlap region is small compared with the physical size of the ADF detector. In terms of Eq. (22) we can say the domain of the \mathbf{K} integral (limited to the disc overlap region) is small compared with the domain of the \mathbf{K}_f integral, and we can make the approximation:

$$I_{\text{ADF}}(\mathbf{Q}) = \int T(\mathbf{K})T^*(\mathbf{K} + \mathbf{Q})d\mathbf{K} \times \int D_{\text{ADF}}(\mathbf{K}_f)\phi(\mathbf{K}_f)\phi^*(\mathbf{K}_f - \mathbf{Q})d\mathbf{K}_f. \quad (24)$$

In making this approximation we have assumed that the contribution of any overlap regions that are partially detected by the ADF detector is small compared with the total signal detected. The integral containing the aperture functions is actually the autocorrelation of the aperture function. The Fourier transform of the probe intensity is the autocorrelation of T , thus Fourier transforming Eq. (24) to give the image results in

$$I(\mathbf{R}_0) = |P(\mathbf{R}_0)| \otimes O(\mathbf{R}_0), \quad (25)$$

where $O(\mathbf{R}_0)$ is the inverse Fourier transform with respect to \mathbf{Q} of the integral over \mathbf{K}_f in Eq. (24).

Equation (25) is the definition of incoherent imaging. The image is regarded as being formed from an object function that is then convolved with a real-positive intensity point-spread function. The Fourier transform of the image will therefore be a product of the Fourier transform of the probe intensity and the Fourier transform of the object function. The Fourier transform of the probe intensity is known as the optical transfer function (OTF) and its typical form is shown in Figure 2-7. Unlike the phase contrast transfer function for BF imaging, it shows no contrast reversals and decays monotonically as a function of spatial frequency.

It is fair to say that the majority of imaging across all radiations can be regarded as incoherent. Generally, an imaged object can be regarded as being effectively self-luminous, which leads directly to an incoherent imaging model (Rayleigh 1896). In this case, the object is not self-luminous, and the illuminating probe is coherent. We noted earlier that the detector geometry can control coherence, and that is exactly what is happening here. Furthermore, by reciprocity, the large annular detector is equivalent to a large (and therefore incoherent) illuminating source, and large sources are another route to ensuring that an imaging process is incoherent.

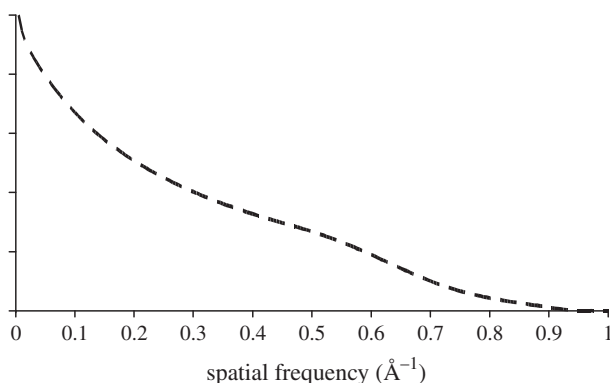


Figure 2-7. A typical optical transfer function (OTF) for incoherent imaging in STEM. This OTF has been calculated for a 300-kV STEM with spherical aberration $C_S = 1$ mm.

Incoherent imaging leads to data that is much easier to interpret. The contrast reversals and delocalization usually associated with HRTEM images are absent, and generally bright features in an ADF image can be associated with the presence of atoms or atomic columns in an aligned crystal. Combined with the strong Z contrast that arises from the high-angle scattering (see Chapter 1) this leads to a high-contrast, chemically sensitive imaging mode. Optimising the conditions for incoherent imaging in STEM is simply a matter of getting the smallest, most intense probe possible. Use of aberrations to generate contrast (as seen in BF imaging) is not required.

As pointed out in Chapter 1, the early investigations suggested that ADF imaging could be regarded as being incoherent only if the all the electrons in the detector plane were summed over, but that this mode would lead to no-image contrast (Ade 1977, Treacy and Gibson 1995). The hole in the ADF detector is therefore crucial to generate contrast, and it is useful to examine its influence on the detector function. By assuming that the maximum image spatial frequency \mathbf{Q} vector is small compared to the geometry of the detector and noting that the detector function is either unity or zero, we can write the Fourier transform of the object function as

$$O(\mathbf{Q}) = \int D_{\text{ADF}}(\mathbf{K}_f) \phi(\mathbf{K}_f) D_{\text{ADF}}(\mathbf{K}_f - \mathbf{Q}) \phi^*(\mathbf{K}_f - \mathbf{Q}) d\mathbf{K}_f. \quad (26)$$

This equation is just the autocorrelation of $D(\mathbf{K})\phi(\mathbf{K})$, and so the object function is

$$O(\mathbf{R}_0) = |D(\mathbf{R}_0) \otimes \phi(\mathbf{R}_0)|^2. \quad (27)$$

Neglecting the outer radius of the detector, where we can assume the strength of the scattering has become negligible, $D(\mathbf{K})$ can be thought of as a sharp high-pass filter. The object function is therefore the modulus squared of the high-pass filtered specimen transmission function.

Nellist and Pennycook (2000) have taken this analysis further by making the weak-phase object approximation, under which condition the object function becomes

$$O(\mathbf{R}_0) = \int_{\text{half plane}} \frac{J_1(2\pi k_{\text{inner}} |\mathbf{R}|)}{2\pi |\mathbf{R}|} \times [\sigma V(\mathbf{R}_0 + \mathbf{R}/2) - \sigma V(\mathbf{R}_0 - \mathbf{R}/2)]^2 d\mathbf{R}, \quad (28)$$

where k_{inner} is the spatial frequency corresponding to the inner radius of the ADF detector, and J_1 is a first-order Bessel function of the first kind. This is essentially the result derived by Jesson and Pennycook (1993). The coherence envelope expected from the Van Cittert–Zernicke theorem is now seen in Eq. (28) as the Airy function involving the Bessel function. If the potential is slowly varying within this coherence envelope, the value of $O(\mathbf{R}_0)$ is small. For $O(\mathbf{R}_0)$ to have significant value, the potential must vary quickly within the coherence envelope. A coherence envelope that is broad enough to include more than one atom in the sample (arising from a small hole in the ADF), however, will show unwanted interference effects between the atoms. Making the coherence envelope too narrow by increasing the inner radius, on the other hand, will lead to too small a variation in the potential within the envelope, and therefore no signal. If there is no hole in the ADF detector, then $D(\mathbf{K}) = 1$ everywhere, and its Fourier transform will be a delta function. Equation (27) then becomes the modulus squared of ϕ , and there will be no contrast. To get signal in an ADF image, we require a hole in the detector, leading to a coherence envelope that is narrow enough to destroy coherence from neighbouring atoms but broad enough to allow enough interference in the scattering from a single atom. In practice, there are further factors that can influence the choice of inner radius, such as the presence of strain contrast. A typical choice for incoherent imaging is that the ADF inner radius should be about three times the objective aperture radius (Hartel et al. 1996), which ensures that the coherence envelope is significantly narrower than the probe.

2.7.1 Incoherent Imaging with Dynamical Diffraction

If one can assume ADF imaging to be incoherent, then it is reasonable to expect that the total scattered intensity would be simply proportional to the number of atoms illuminated by the probe. Early applications of ADF imaging showed that diffraction of the electron beam in the sample could still influence the intensity seen in ADF images (Donald and Craven 1979). Specifically, when a crystal is aligned with a low-order zone axis parallel to the beam, strong channelling conditions which enhance the strength of the scattering to high angles are established. To explain this, we need to examine the influence of dynamical diffraction.

The analysis performed above has assumed that the scattering by the sample can be treated as being a simple, multiplicative transmission

function, i.e. the sample is thin. Under dynamical diffraction conditions, the multiplicative transmission function approximation cannot be made. If we continue to neglect thermal diffuse scattering (which we include in Section 2.7.3), then it is possible to include dynamical diffraction by making use of the Bloch wave model. In Eq. (22), the Fourier transform of the object function gives the strength of the scattering from an incoming partial plane wave to an outgoing one. The effect of dynamical diffraction is that the strength of the scattering is no longer simply dependent on the change of wavevector but on the incoming and outgoing wavevectors independently, thus

$$I_{\text{ADF}}(\mathbf{Q}, z) = \iint D_{\text{ADF}}(\mathbf{K}_f) T(\mathbf{K}) T^*(\mathbf{K} + \mathbf{Q}) \times \phi(\mathbf{K}_f, \mathbf{K}, z) \phi^*(\mathbf{K}_f, \mathbf{K} - \mathbf{Q}, z) d\mathbf{K}_f d\mathbf{K}. \quad (29)$$

To include the effects of dynamical scattering, in a perfect crystal that only contains spatial frequencies corresponding to reciprocal lattice points it is possible to follow the approach of Nellist and Pennycook (1999) and write the scattering as a sum over Bloch waves (see, for example, Humphreys and Bithell 1992):

$$\begin{aligned} \tilde{I}_{\text{ADF}}(\mathbf{Q}, z) = & \sum_{\mathbf{g}} D_{\text{ADF}}(\mathbf{g}) \int T(\mathbf{K}) T^*(\mathbf{K} + \mathbf{Q}) \\ & \times \sum_j \Phi_0^{(j)*}(\mathbf{K}) \Phi_{\mathbf{g}}^{(j)}(\mathbf{K}) \exp \left[-i2\pi z k_z^{(j)}(\mathbf{K}) \right] \\ & \times \sum_k \Phi_{\mathbf{Q}}^{(k)}(\mathbf{K}) \Phi_{\mathbf{g}}^{(k)*}(\mathbf{K}) \exp \left[i2\pi z k_z^{(k)}(\mathbf{K}) \right] d\mathbf{K}, \end{aligned} \quad (30)$$

where $\Phi_{\mathbf{g}}^{(j)}(\mathbf{K})$ is the \mathbf{g} th Fourier component of the j th Bloch wave for an incoming beam with transverse wavevector \mathbf{K} . By performing the \mathbf{g} summation first, which plays an equivalent role in the sum over the detector in Eq. (22), it is possible to look at the degree of coherent interference between different Bloch waves, thus

$$C_{ij}(\mathbf{K}) = \sum_{\mathbf{g}} D_{\text{ADF}}(\mathbf{g}) \Phi_{\mathbf{g}}^{(j)}(\mathbf{K}) \Phi_{\mathbf{g}}^{(k)*}(\mathbf{K}), \quad (31)$$

which, in a similar fashion to the approach in Eq. (28), can be written in terms of the hole in the detector:

$$C_{ij}(\mathbf{K}') = \delta_{ij} - \int \frac{J_1(2\pi u_{\text{in}} |\mathbf{B}|)}{2\pi |\mathbf{B}|} \int \Phi^{(j)}(\mathbf{C}, \mathbf{K}) \Phi^{(k)*}(\mathbf{C} + \mathbf{B}, \mathbf{K}) d\mathbf{C} d\mathbf{B}, \quad (32)$$

where \mathbf{B} and \mathbf{C} are dummy real-space variables of integration, and the Bloch waves have been written as real-space functions for a given incident beam transverse wavevector \mathbf{K} . As we saw before, the hole in the detector is imposing a coherence envelope. Thus $C_{jk}(\mathbf{K})$ allows only interference effects to show up in the ADF image between Bloch states that are sharply peaked and whose peaks are physically close such that they lie within a few tenths of an angstrom of each other. A physical interpretation is that the high-angle ADF detector is acting like a high-pass filter (as it has been seen to do for thin specimens – see Section 2.7.1) acting on the exit-surface wavefunction. Only when the probe

excites sharply peaked Bloch states will the electron density be sharply peaked.

2.7.2 The Effect of Thermal Diffuse Scattering

Early analyses of ADF imaging took the approach that at high enough scattering angles, the thermal diffuse scattering (TDS) arising from phonons would dominate the image contrast (Howie 1979). In the Einstein approximation, this scattering is completely uncorrelated between atoms, and therefore there could be no coherent interference effects between the scattering from different atoms. In this approach the intensity of the wavefunction at each site needs to be computed using a dynamical elastic scattering model and then the TDS from each atom summed (Allen et al. 2003, Pennycook and Jesson 1990). When the probe is located over an atomic column in the crystal, the most bound, least dispersive states (usually 1s or 2s-like) are predominantly excited and the electron intensity “channels” down the column. This channelling effect reduces the spreading of the probe as it propagates, which is useful for thicker samples, though spreading can still be seen, especially for aberration-corrected instruments with larger convergence angles (Dwyer and Etheridge 2003). When the probe is not located over a column, it excites more dispersive, less bound states and spreads leading to reduced intensity at the atom sites and a lower ADF signal. Both the Bloch wave (for example Amali and Rez 1997, Findlay et al. 2003, Mitsuishi et al. 2001, Pennycook 1989) and multislice (for example Allen et al. 2003, Dinges et al. 1995, Kirkland et al. 1987, Loane et al. 1991) methods have been used for simulating the TDS scattering to the ADF detector. Details of the way TDS is incorporated into image calculations can be found in Chapter 6.

It is possible to see the incoherence due to the detector geometry and the incoherence due to TDS in a similar framework. In the analyses presented here, the key to incoherent imaging has been the sum over the many final wavevectors that are incident upon the detector. One way of explaining the diffuse nature of thermal scattering is to consider that, in addition to the transverse momentum imparted by the elastic scattering from the crystal, additional momentum is imparted by scattering from a phonon. Phonon momenta will be comparable to reciprocal lattice vectors, and the range of phonon momenta present in a crystal will therefore blur the elastic diffraction pattern. Furthermore, each phonon will impart a slightly different energy to others, and therefore scattering by different phonon momenta will lead to waves that are mutually incoherent. If we consider a single detection point, many beams elastically scattered to different final wavevectors will be additionally scattered by phonons to the detector, leading to a sum in intensity over final elastic wavevectors – exactly what is required for incoherent imaging. It is fair to say, however, that the geometry of the ADF detector will always be larger than typical phonon momenta (not least because longer wavelength phonons are usually more common) and that transverse incoherence is ensured by the use of a large detector. It is interesting to speculate whether a small detector at high angle

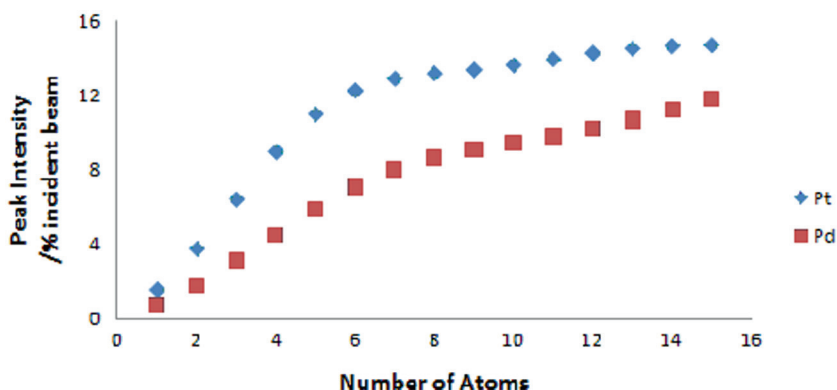


Figure 2-8. The peak ADF image intensity (expressed as a fraction of the incident beam current) for isolated Pt and Pd columns expressed as a function of number of atoms in a column (graph courtesy of H. E).

would give a strongly incoherent signal, relying as it would purely on the sum over phonon momenta to give the necessary integral to destroy the coherence.

The combined effects of channelling and TDS give rise to a dependence of ADF image peak intensity on sample thickness typically of the form shown in Figure 2-8. The ADF signal rises monotonically with thickness, but is clearly non-linear, and so is not proportional to the number of illuminated atoms. Changes in the slope of the graph are caused by variations in the strength of the electron beam channelling along the column, arising from both channelling oscillations and absorption. It is therefore clear that quantitative interpretation of ADF images does require matching to simulations.

Almost all the simulations currently performed assume an Einstein phonon dispersion model. Other, more realistic, dispersions have been considered (Jesson and Pennycook 1995). Although the detector geometry is highly effective for destroying coherence perpendicular to the beam direction, phonons play a much more important role in controlling the coherence parallel to the beam direction. Jesson and Pennycook (1995) showed that a realistic phonon dispersion could give rise to short-range coherence envelopes in the depth direction. Detailed multislice simulations (Muller et al. 2001) suggest that the effect of a realistic phonon dispersion on the ADF intensities for a perfect crystal is small.

The combination of channelling and absorption can also lead to some unexpected effects when the displacement of atoms varies along a column, referred to as strain contrast. Strain can lead to either a depletion or an enhancement of ADF intensities depending on the inner radius of the detector (Yu et al. 2004). This phenomenon has been ascribed to the strain causing interband scattering between Bloch waves (Perovic et al. 1993). A channelling wave that has been strongly absorbed may be replenished by interband scattering, thereby leading to increased intensity.

2.8 Imaging Using Inelastic Electrons

Using the STEM to image at, or close to, atomic resolution using inelastically scattered electrons is a powerful experimental mode. Remarkable progress has been made since it was first demonstrated (Browning et al. 1993) and the development of aberration-corrected STEM has allowed impressive atomic-resolution mapping to be demonstrated. Only core-loss inelastic scattering provides a sufficiently localized signal to allow atomic resolution, and because such scattering involves the excitation of an atomic core state to a final state, it is clear that such scattering will be independent of neighbouring atoms and that no interference between the scattering from neighbouring atoms can be expected.

The inclusion of inelastic scattering is discussed extensively in Chapter 6. As shown there, scattering from a specific initial state to a specific final state can be treated by a simple, multiplicative scattering function (see Eq. (11) of Chapter 6). The final image will be a sum in intensity over many of such scattering functions because for any experiment with finite energy resolution, a significant number of final states must be included. Because each final state differs slightly in energy, a sum in intensity is required, thereby breaking the coherence in the imaging process. As noted in Chapter 6, however, this summation is often not sufficient to prevent partial coherence effects from being observed, and the use of a large collector aperture is further required to ensure incoherent imaging. A large collector aperture destroys coherence in exactly the same way as the large ADF detector does for elastic or quasi-elastic scattering.

2.9 Optical Depth Sectioning and Confocal Microscopy

So far we have considered only two-dimensional imaging. The development of aberration correctors in STEM has led to dramatic improvements in lateral resolution due to the larger objective lens numerical aperture allowed. Whilst the lateral resolution varies as the inverse of the numerical aperture, the depth of focus is inversely proportional to the square of the numerical aperture. In a state-of-the-art, aberration-corrected STEM, the depth of focus may fall to just a few nanometres, which is less than the typical thickness of TEM samples. The full width at half-maximum of the probe intensity along the optic axis is given by

$$\Delta z = 1.77 \frac{\lambda}{\alpha^2}. \quad (33)$$

Whilst this raises concerns about interpreting high-resolution images from thicker samples, it does raise the possibility of using this reduced depth of focus to retrieve depth information.

The simplest approach to measuring such 3D information in STEM is to record a focal series of images, thereby forming a 3D stack. Clearly we want an incoherent imaging mode where the scattering is simply

dependent on the 3D probe intensity distribution, and ADF imaging is therefore suitable. Such an approach has been used for the 3D imaging of Hf atoms in a transistor gate oxide stack (Van Benthem et al. 2005). Applications to the mapping of nanoparticle locations in heterogeneous catalysts (Borisevich et al. 2006) showed significant elongation in the depth direction. This elongation was subsequently investigated by Behan et al. (2009) and was seen to arise from the form of the OTF in three dimensions. Figure 2–7 has already shown the form of the OTF in 2D, and a 3D OTF can simply be formed by taking the Fourier transform of the 3D probe intensity distribution. As seen in Figure 2–9, the OTF is approximately of a donut shape and has a large missing region. This missing region is known from light optics (Frieden 1967) and has an opening angle that is given by $90^\circ - \alpha$, where α is the acceptance angle of the lens. In light optics, α can approach close to 90° , whereas even in an aberration-corrected STEM, α is less than 2° , leading to a large missing region in the OTF. For laterally extended objects that are dominated by low transverse spatial frequencies, only low longitudinal spatial frequencies will be transferred, leading to longitudinal elongation. The depth resolution for an extended object can be approximated as

$$\Delta z = \frac{d}{\alpha}, \quad (34)$$

where d is the lateral extent of the object. Even for a 5-nm particle, the depth resolution in an aberration-corrected STEM would be typically 200 nm. Methods to use deconvolution to overcome this problem have been investigated (Behan et al. 2009, de Jonge et al. 2010), but it must be

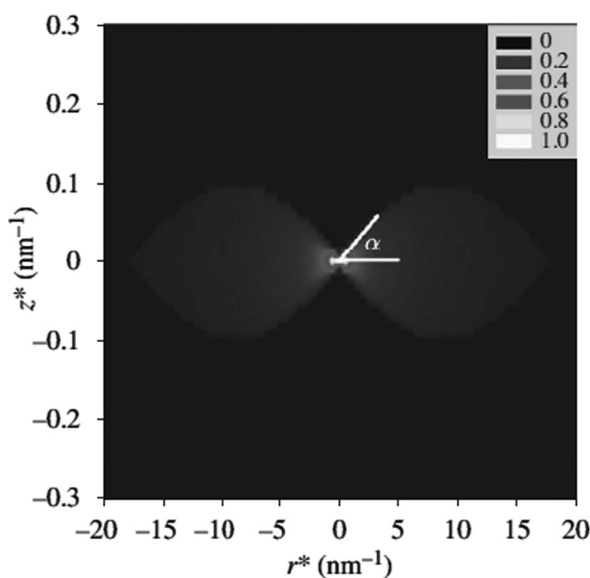


Figure 2–9. A cross section through the 3D OTF for incoherent imaging. Note the missing cone region. The longitudinal (z^*) and lateral (r^*) axes have different scales. A 200-kV microscope with $\alpha = 22$ mrad has been assumed. Reproduced from Behan et al. (2009).

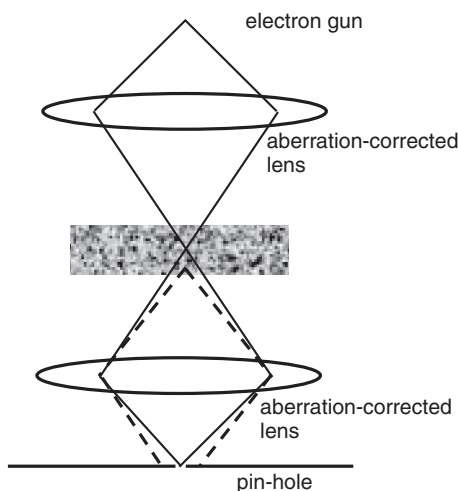


Figure 2–10. A schematic of the scanning confocal electron microscope. Scattering from regions of the sample away from the confocal point (*dashed lines*) is neither strongly illuminated nor focused at the detector pinhole.

remembered that it is not possible to reconstruct the information in the missing cone unless prior information is included.

It has recently been shown that it is possible to use a microscope fitted with aberration correctors both before and after the sample in a confocal geometry (Nellist et al. 2006), similar to the confocal scanning optical microscope that is widely used in light optics (Figure 2–10). The advantage of such a configuration is that the second lens provides additional depth resolution and selectivity. Further detailed analysis of SCEM image contrast has been performed for both elastic (Cosgriff et al. 2008) and inelastic (D’Alfonso et al. 2008) scattering. For elastic scattering, there is no first-order phase contrast transfer, and so the contrast is weak and relies on multiple scattering. Collection of inelastic scattering, in the energy-filtered SCEM (EFSCEM) mode, is much more promising (see also Chapter 6). There is no missing cone in the transfer function (Figure 2–11) and recent results suggest that nanoscale depth resolutions are achievable from laterally extended objects (Wang et al. 2010).

2.10 Conclusions

In this chapter we have reviewed imaging in the STEM, with particular focus on BF and ADF imaging. A key strength of ADF imaging is its incoherent nature, which it shares with many other STEM signals such as EELS and EDX. Unlike conventional high-resolution TEM, the main requirement for STEM is to minimize the aberrations so that a small, intense probe is formed.

In this chapter we concentrated on single signals (e.g. BF or ADF) that are recorded as a function of probe position. Large areas of the

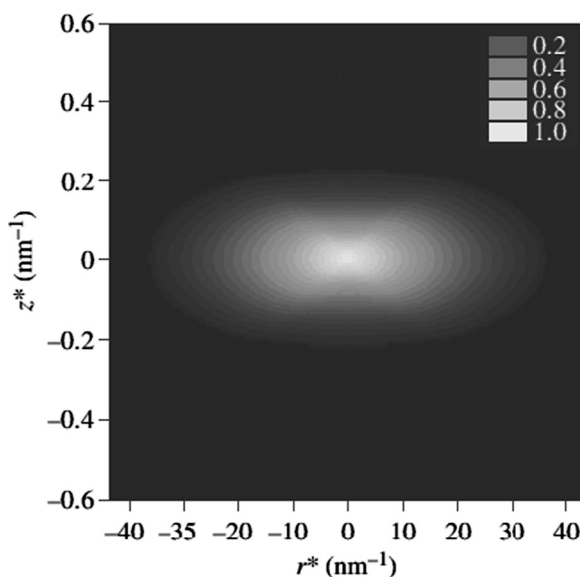


Figure 2-11. A cross section through the transfer function for incoherent SCEM imaging. A 200-kV microscope with both the pre- and post-specimen optics subtending 22 mrad has been assumed. Reproduced from Behan et al. (2009).

detector plane are summed over to record these signals, thus discarding significant amounts of information. Attempts have been made to use position-sensitive detectors in STEM imaging (see, for example, Nellist et al. 1995, Rodenburg and Bates 1992) but have been limited to rather small fields of view because of the problems of acquiring and handling the vast amounts of data. With improved detectors and information technology, we may well see a re-emergence of the idea of collecting the entire detector plane as a function of each probe position (for some recent ideas, see Faulkner and Rodenburg 2004). All possible detector geometries can then be synthesized, or the entire 4D data set used to retrieve information about the sample.

Acknowledgements The author would like to thank the many colleagues and collaborators that have been involved in furthering our understanding of STEM imaging. P.D.N. acknowledges support from the Leverhulme Trust (F/08749/B), Intel Ireland, and the Engineering and Physical Sciences Research Council (EP/F048009/1).

References

- G. Ade, On the incoherent imaging in the scanning transmission electron microscope. *Optik* **49**, 113–116 (1977)
- L.J. Allen, S.D. Findlay, M.P. Oxley, C.J. Rossouw, Lattice-resolution contrast from a focused coherent electron probe. Part I. *Ultramicroscopy* **96**, 47–63 (2003)
- A. Amali, P. Rez, Theory of lattice resolution in high-angle annular dark-field images. *Microsc. Microanal.* **3**, 28–46 (1997)

- G. Behan, E.C. Cosgriff, A.I. Kirkland, P.D. Nellist, Three-dimensional imaging by optical sectioning in the aberration-corrected scanning transmission electron microscope. *Philos. Trans. R. Soc. Lond. A* **367**, 3825–3844 (2009)
- A.Y. Borisevich, A.R. Lupini, S.J. Pennycook, Depth sectioning with the aberration-corrected scanning transmission electron microscope. *Proc. Natl. Acad. Sci.* **103**, 3044–3048 (2006)
- N.D. Browning, M.F. Chisholm, S.J. Pennycook, Atomic-resolution chemical analysis using a scanning transmission electron microscope. *Nature* **366**, 143–146 (1993)
- E.C. Cosgriff, A.J. D’Alfonso, L.J. Allen, S.D. Findlay, A.I. Kirkland, P.D. Nellist, Three dimensional imaging in double aberration-corrected scanning confocal electron microscopy. Part I: Elastic scattering. *Ultramicroscopy* **108**, 1558–1566 (2008)
- J.M. Cowley, Image contrast in a transmission scanning electron microscope. *Appl. Phys. Lett.* **15**, 58–59 (1969)
- J.M. Cowley, Coherent interference in convergent-beam electron diffraction & shadow imaging. *Ultramicroscopy* **4**, 435–450 (1979)
- J.M. Cowley, Coherent interference effects in SIEM and CBED. *Ultramicroscopy* **7**, 19–26 (1981)
- A.V. Crewe, The physics of the high-resolution STEM. *Rep. Progr. Phys.* **43**, 621–639 (1980)
- A.V. Crewe, D.N. Eggenberger, J. Wall, L.M. Welter, Electron gun using a field emission source. *Rev. Sci. Instrum.* **39**, 576–583 (1968)
- A.V. Crewe, J. Wall, A scanning microscope with 5 Å resolution. *J. Mol. Biol.* **48**, 375–393 (1970)
- A.J. D’Alfonso, E.C. Cosgriff, S.D. Findlay, G. Behan, A.I. Kirkland, P.D. Nellist, L.J. Allen, Three dimensional imaging in double aberration-corrected scanning confocal electron microscopy. Part II: Inelastic scattering. *Ultramicroscopy* **108**, 1567–1578 (2008)
- N. de Jonge, R. Sougrat, B.M. Northan, S.J. Pennycook, Three-dimensional scanning transmission electron microscopy of biological specimens. *Microsc. Microanal.* **16**, 54–63 (2010)
- N.H. Dekkers, H. de Lang, Differential phase contrast in a STEM. *Optik* **41**, 452–456 (1974)
- C. Dinges, A. Berger, H. Rose, Simulation of TEM images considering phonon and electron excitations. *Ultramicroscopy* **60**, 49–70 (1995)
- A.M. Donald, A.J. Craven, A study of grain boundary segregation in Cu–Bi alloys using STEM. *Philos. Mag. A* **39**, 1–11 (1979)
- C. Dwyer, J. Etheridge, Scattering of Å-scale electron probes in silicon. *Ultramicroscopy* **96**, 343–360 (2003)
- H.M.L. Faulkner, J.M. Rodenburg, Moveable aperture lensless transmission microscopy: A novel phase retrieval algorithm. *Phys. Rev. Lett.* **93**, 023903 (2004)
- S.D. Findlay, L.J. Allen, M.P. Oxley, C.J. Rossouw, Lattice-resolution contrast from a focused coherent electron probe. Part II. *Ultramicroscopy* **96**, 65–81 (2003)
- B.R. Frieden, Optical transfer of the three-dimensional object. *J. Opt. Soc. Am.* **57**, 36–41 (1967)
- S.J. Haigh, H. Sawada, A.I. Kirkland, Atomic structure imaging beyond conventional resolution limits in the transmission electron microscope. *Phys. Rev. Lett.* **103**, 126101 (2009)
- P. Hartel, H. Rose, C. Dinges, Conditions and reasons for incoherent imaging in STEM. *Ultramicroscopy* **63**, 93–114 (1996)
- A. Howie, Image contrast and localised signal selection techniques. *J. Microsc.* **117**, 11–23 (1979)

- C.J. Humphreys, E.G. Bithell, in *Electron Diffraction Techniques*, vol. 1, ed. by J.M. Cowley (OUP, New York, NY, 1992), pp. 75–151
- D.E. Jesson, S.J. Pennycook, Incoherent imaging of thin specimens using coherently scattered electrons. *Proc. R. Soc. (Lond.) Ser. A* **441**, 261–281 (1993)
- D.E. Jesson, S.J. Pennycook, Incoherent imaging of crystals using thermally scattered electrons. *Proc. Roy. Soc. (Lond.) Ser. A* **449**, 273–293 (1995)
- E.J. Kirkland, R.F. Loane, J. Silcox, Simulation of annular dark field STEM images using a modified multislice method. *Ultramicroscopy* **23**, 77–96 (1987)
- R.F. Loane, P. Xu, J. Silcox, Thermal vibrations in convergent-beam electron diffraction. *Acta Crystallogr. A* **47**, 267–278 (1991)
- R.F. Loane, P. Xu, J. Silcox, Incoherent imaging of zone axis crystals with ADF STEM. *Ultramicroscopy* **40**, 121–138 (1992)
- K. Mitsuishi, M. Takeguchi, H. Yasuda, K. Furuya, New scheme for calculation of annular dark-field STEM image including both elastically diffracted and TDS wave. *J. Electron Microsc.* **50**, 157–162 (2001)
- D.A. Muller, B. Edwards, E.J. Kirkland, J. Silcox, Simulation of thermal diffuse scattering including a detailed phonon dispersion curve. *Ultramicroscopy* **86**, 371–380 (2001)
- P.D. Nellist, G. Behan, A.I. Kirkland, C.J.D. Hetherington, Confocal operation of a transmission electron microscope with two aberration correctors. *Appl. Phys. Lett.* **89**, 124105 (2006)
- P.D. Nellist, B.C. McCallum, J.M. Rodenburg, Resolution beyond the ‘information limit’ in transmission electron microscopy. *Nature* **374**, 630–632 (1995)
- P.D. Nellist, S.J. Pennycook, Accurate structure determination from image reconstruction in ADF STEM. *J. Microsc.* **190**, 159–170 (1998)
- P.D. Nellist, S.J. Pennycook, Subangstrom resolution by underfocussed incoherent transmission electron microscopy. *Phys. Rev. Lett.* **81**, 4156–4159 (1998)
- P.D. Nellist, S.J. Pennycook, Incoherent imaging using dynamically scattered coherent electrons. *Ultramicroscopy* **78**, 111–124 (1999)
- P.D. Nellist, S.J. Pennycook, The principles and interpretation of annular dark-field Z-contrast imaging. *Adv. Imag. Electron Phys.* **113**, 148–203 (2000)
- P.D. Nellist, J.M. Rodenburg, Beyond the conventional information limit: the relevant coherence function. *Ultramicroscopy* **54**, 61–74 (1994)
- S.J. Pennycook, Z-contrast STEM for materials science. *Ultramicroscopy* **30**, 58–69 (1989)
- S.J. Pennycook, D.E. Jesson, High-resolution incoherent imaging of crystals. *Phys. Rev. Lett.* **64**, 938–941 (1990)
- D.D. Perovic, C.J. Rossouw, A. Howie, Imaging elastic strain in high-angle annular dark-field scanning transmission electron microscopy. *Ultramicroscopy* **52**, 353–359 (1993)
- Lord Rayleigh, On the theory of optical images with special reference to the microscope. *Philos. Mag.* **42**(5), 167–195 (1896)
- J.M. Rodenburg, R.H.T. Bates, The theory of super-resolution electron microscopy via Wigner-distribution deconvolution. *Philos. Trans. R. Soc. Lond. A* **339**, 521–553 (1992)
- H. Rose, Phase contrast in scanning transmission electron microscopy. *Optik* **39**, 416–436 (1974)
- J.C.H. Spence, *Experimental High-Resolution Electron Microscopy* (OUP, New York, NY, 1988)
- J.C.H. Spence, Convergent-beam nanodiffraction, in-line holography and coherent shadow imaging. *Optik* **92**, 57–68 (1992)

- J.C.H. Spence, J.M. Cowley, Lattice imaging in STEM. *Optik* **50**, 129–142 (1978)
- M.M.J. Treacy, J.M. Gibson, Atomic contrast transfer in annular dark-field images. *J. Microsc.* **180**, 2–11 (1995)
- M.M.J. Treacy, A. Howie, C.J. Wilson, Z contrast imaging of platinum and palladium catalysts. *Philos. Mag. A* **38**, 569–585 (1978)
- K. Van Benthem, A.R. Lupini, M. Kim, H.S. Baik, S. Doh, J.-H. Lee, M.P. Oxley, S.D. Findlay, L.J. Allen, J.T. Luck, S.J. Pennycook, Three-dimensional imaging of individual hafnium atoms inside a semiconductor device. *Appl. Phys. Lett.* **87**, 034104 (2005)
- P. Wang, G. Behan, M. Takeguchi, A. Hashimoto, K. Mitsuishi, M. Shimojo, A.I. Kirkland, P.D. Nellist, Nanoscale energy-filtered scanning confocal electron microscopy using a double-aberration-corrected transmission electron microscope. *Phys. Rev. Lett.* **104**, 200801 (2010)
- Z. Yu, D.A. Muller, J. Silcox, Study of strain fields at a-Si/c-Si interface. *J. Appl. Phys.* **95**, 3362–3371 (2004)
- E. Zeitler, M.G.R. Thomson, Scanning transmission electron microscopy. *Optik* **31**, 258–280 and 359–366 (1970)

Scanning Transmission Electron Microscopy
Imaging and Analysis

Pennycook, S.J.; Nellist, P.D. (Eds.)

2011, XII, 762 p., Hardcover

ISBN: 978-1-4419-7199-9